JOURNAL OF PROPULSION AND POWER
Vol. 21, No. 4, July–August 2005

Blunt-Body Generated Detonation in Viscous Hypersonic Ducted Flows

P. R. Ess*
University of Bristol, Bristol, England BS8 1TR, United Kingdom
J. P. Sislian†
University of Toronto, Toronto, Ontario M3H 5T6, Canada
and
C. B. Allen‡
University of Bristol, Bristol, England BS8 1TR, United Kingdom

Heat release from detonation waves due to blunt bodies embedded into a constant area channel flow was studied numerically, solving laminar Navier–Stokes equations for chemically reacting nonequilibrium flows with a steady-state and time-accurate formulation. A maximum heat release is of interest in the context of propulsion applications, where the energy added to the flow can be utilized to increase thrust. Hence, channel blockage ratios (CBR), defined as the ratio of blunt-body diameter over channel height, in the range from 1/18 to 1/3 were examined for inflow conditions typical for a shock-induced combustion ramjet combustor of a hypersonic vehicle operating in a flight altitude of 38 km and a Mach number in excess of 10. The flow entering the domain at Mach number 5 is a stoichiometrically premixed hydrogen–air gas mixture that was modeled with 13 species and 33 chemical reaction equations.

Nomenclature

c_p	=	heat coefficient per unit mass at constant pressure, J/(kg · K)
c_v	=	heat coefficient per unit mass at constant volume, J/(kg · K)
D	=	blunt-body diameter, m
$D_{i,j}$	=	binary diffusion coefficient, m^2/s
E	=	total energy per unit mass, J/kg
e	=	internal energy per unit mass, J/kg
$\boldsymbol{F}, \boldsymbol{G}, \boldsymbol{H}$	=	flux vectors
H	=	channel height, m
h	=	enthalpy, J/kg
$\underline{\boldsymbol{I}}$	=	identity matrix
$\boldsymbol{j}$	=	diffusion flux vector
M	=	molecular weight, kg/kmol
Ma	=	Mach number
N_s	=	number of species
$\boldsymbol{n}$	=	cell side normal vector
p	=	pressure, Pa
$\boldsymbol{Q}$	=	vector of conserved variables
$\boldsymbol{R}$	=	right-hand side, residual vector
Re	=	Reynolds number
R^*	=	universal gas constant, J/(kmol · K)
$\boldsymbol{S}$	=	source term vector
T	=	temperature, K
Th	=	thrust potential, N · s/kg, m/s
t	=	time, s
u, v	=	x and y components of velocity, m/s
V	=	control volume, m^3
X_i	=	molar fraction of component i
x, y	=	x and y radial coordinate, m
Y_i	=	mass fraction of component i
Γ	=	control surface
γ	=	ratio of specific heats
Δh_r	=	heat of reaction, J/kg
ε	=	error, normalized residual
$\boldsymbol{\varepsilon}$	=	energy flux vector
$\tilde{\epsilon}, \epsilon$	=	entropy correction and its coefficient
Λ	=	spectral radius (largest absolute eigenvalue of matrix)
λ	=	heat conductivity, J/(s · m · K)
μ	=	kinematic viscosity, kg/(m · s)
ρ	=	density, kg/m^3
$\underline{\boldsymbol{\tau}}$	=	stress tensor
ω	=	chemical source term, $kg/(m^3 \cdot s)$

Introduction

SHOCK-INDUCED combustion ramjets, or shcramjets, recently emerged as an alternative hypersonic propulsion system to scramjets. As its name indicates, heat addition to a supersonic flow, in this mode, is accomplished through a conveniently located shock that ignites the combustible mixture premixed ahead of the combustion inducing shock in the forebody/inlet of the vehicle. Under the assumption that this premixing is achieved satisfactorily, most, if not all, of the research work on shcramjets has considered sharp-wedge generated oblique detonation or shock-induced combustion mechanism of heat addition. An overview of previous research on shcramjets can be found in Ref. 1. Oblique detonation waves exhibit minimum entropy rise or total pressure loss and maximum heat release when they are operated at near Chapman–Jouguet conditions. In addition to concerns about the stability of such a standing detonation wave configuration, Chapman–Jouguet detonation waves exhibit a notable ignition induction distance near the wedge surface that may causes problems at off-design operating conditions because induction lengths are very sensitive to temperature variations.

Received 3 October 2003; revision received 23 November 2004; accepted for publication 23 November 2004.

*Graduate Student, Department of Aerospace Engineering; currently Research Associate, Department of Aeronautics, Prince Consort Road, Imperial College London, London, England SW7 2BY, U.K. Member AIAA.
†Professor, Institute for Aerospace Studies. Associate Fellow AIAA.
‡Reader, Department of Aerospace Engineering, Queen's Building, University Walk. Member AIAA.

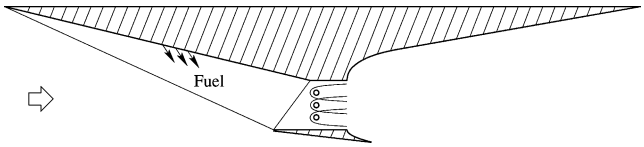

Fig. 1 Scramjet with blunt-body generated combustion.

This concern about the initiation and stability of sharp-wedge induced detonation waves over a range of flight conditions has motivated the consideration of the alternative means of heat addition to a premixed supersonic combustible flow by blunt-body generated detonations. The initiation and stability of detonation waves generated by a single blunt body in an unbounded supersonic combustible mixture has been the subject of extensive investigation by many researchers. (See Ref. 2 for the relevant scientific literature.) Experiments based on axisymmetric projectiles fired into premixed, combustible gas were performed by, for instance, Lehr[3] for hydrogen–air and Kasahara et al.[4] for hydrogen–oxygen mixtures, to study regimes of shock-induced combustion and detonation.

The present paper is concerned with blunt-body generated detonation waves in a ducted supersonic combustible flow, a possible proposed use of blunt bodies, namely, cylindrical rods placed normal to the local flow direction in the propulsive duct of a shcramjet, as shown in Fig. 1. For high supersonic velocities and enthalpies of the incoming flow characteristic of hypersonic propulsive devices, the advantage this configuration promises over sharp-wedge generated oblique detonation waves are guaranteed combustion due to strong shocks formed in front of the blunt body, shorter combustion lengths, and, possibly, better off-design performance of the combustor. Obviously, the implications blunt-body generated combustion would have on the overall shcramjet engine performance are of vital importance in assessing the feasibility of such a concept. Under the assumption that the duct, that is, combustor, height is fixed, the objective here is to investigate numerically the formation and stability of the resulting different flow configurations in function of the blockage ratio, diameter of the rod to duct height, and to determine the blockage ratio that results in minimum losses and maximum heat addition to the ducted flow.

After the introduction of the governing equations, the numerical method and its validation are presented. Subsequently, the setup for the study of blunt-body generated combustion is defined, and the results obtained by the numerical method are shown and discussed. Finally, some conclusions are drawn and an outlook to future work given.

Governing Equations

By the use of density ρ, velocities u and v, pressure p, total energy E, species mass fraction Y, chemical source term ω, shear stress τ, diffusion and energy fluxes $\boldsymbol{j}$ and $\boldsymbol{\epsilon}$, and axial and radial coordinates x and y, the axisymmetric, laminar Navier–Stokes equations for a chemically reacting multispecies gas flow with N_s components are given in conservative, differential form by

$$\frac{\partial}{\partial t}\boldsymbol{Q} + \frac{\partial}{\partial x}(\boldsymbol{G}_c - \boldsymbol{G}_d) + \frac{1}{y}\frac{\partial}{\partial y}y(\boldsymbol{H}_c - \boldsymbol{H}_d) = \boldsymbol{S} \tag{1}$$

with

$$\boldsymbol{Q} = \begin{bmatrix} \rho \\ \rho u \\ \rho v \\ \rho E \\ \rho Y_1 \\ \vdots \\ \rho Y_{N_s-1} \end{bmatrix}, \qquad \boldsymbol{S} = \begin{bmatrix} 0 \\ 0 \\ \dfrac{p}{y} - \dfrac{\tau_{\theta\theta}}{y} \\ 0 \\ \omega_1 \\ \vdots \\ \omega_{N_s-1} \end{bmatrix}$$

$$\boldsymbol{G}_c = \begin{bmatrix} \rho u \\ \rho u^2 + p \\ \rho uv \\ u(\rho E + p) \\ \rho u Y_1 \\ \vdots \\ \rho u Y_{N_s-1} \end{bmatrix}, \qquad \boldsymbol{H}_c = \begin{bmatrix} \rho v \\ \rho uv \\ \rho v^2 + p \\ v(\rho E + p) \\ \rho v Y_1 \\ \vdots \\ \rho v Y_{N_s-1} \end{bmatrix}$$

$$\boldsymbol{G}_d = \begin{bmatrix} 0 \\ \tau_{xx} \\ \tau_{xy} \\ u\tau_{xx} + v\tau_{xy} - \epsilon_x \\ -j_{x_1} \\ \vdots \\ -j_{x_{N_s-1}} \end{bmatrix}, \qquad \boldsymbol{H}_d = \begin{bmatrix} 0 \\ \tau_{yx} \\ \tau_{yy} \\ u\tau_{xy} + v\tau_{yy} - \epsilon_y \\ -j_{y_1} \\ \vdots \\ -j_{y_{N_s-1}} \end{bmatrix}$$

where

$$\tau_{xx} = \frac{2}{3}\mu\left(2\frac{\partial u}{\partial x} - \frac{\partial v}{\partial y} - \frac{v}{y}\right) \tag{2}$$

$$\tau_{yy} = \frac{2}{3}\mu\left(2\frac{\partial v}{\partial y} - \frac{\partial u}{\partial x} - \frac{v}{y}\right) \tag{3}$$

$$\tau_{xy} = \mu\left(\frac{\partial u}{\partial y} + \frac{\partial v}{\partial x}\right) \tag{4}$$

$$\tau_{\theta\theta} = \frac{2}{3}\mu\left(2\frac{v}{y} - \frac{\partial v}{\partial y} - \frac{\partial u}{\partial x}\right) \tag{5}$$

and μ is the viscosity of the gas mixture. The species diffusion was calculated using Fick's law, where the diffusion coefficient $D_{i,\text{mix}}$ for species i with respect to the gas mixture replaces the binary diffusion coefficients (see Ref. 5)

$$\boldsymbol{j}_i = -\rho D_{i,\text{mix}} \nabla Y_i \tag{6}$$

Fick's law is an approximation of the multicomponent diffusion equations obtained from the kinetic theory of gases, which significantly reduces the computational costs of diffusion flux calculation. The validity of this approximation was discussed by Williams.[6]

Furthermore, the energy flux vector was calculated by summarizing heat conduction and enthalpy diffusion according to

$$\boldsymbol{\epsilon} = -\lambda \nabla T + \sum_{i=1}^{N_s} h_i \boldsymbol{j}_i \tag{7}$$

where λ is the heat conductivity coefficient. Finite rate chemistry using the extended Arrhenius equation to calculate the reaction rates is employed to calculate the chemical source terms ω_i.

Thermodynamic closure of the system of equations is achieved by the thermal equation of state for a multispecies gas

$$p = \rho RT = \rho R^* T \sum_{i=1}^{N_s} \frac{Y_i}{M_i} \tag{8}$$

with R^* as the universal gas constant and $R = R^*/M$ as the gas constant for the mixture. Furthermore, the enthalpy of the gas mixture was calculated according to

$$h = \sum_{i=1}^{N_s} Y_i h_i = \sum_{i=1}^{N_s} Y_i \left(h_{fi}^0 + \int_{T_{\text{ref}}}^{T} c_{p_i}\, \mathrm{d}T\right) \tag{9}$$

where h_{fi}^0 is the heat of formation at the given reference temperature T_{ref}. The specific heats at constant pressure c_{p_i} were computed

using polynomials with appropriate coefficients provided by McBride et al.[7]

The transport properties' viscosity, thermal conductivity, and binary diffusion coefficients are calculated for each species following the laws of kinetic gas theory.[8] Next, mixing rules are applied to obtain the appropriate properties for the multispecies gas up to a 5–10% accuracy, as outlined by Warnatz and Maas.[5]

For the reproduction of Lehr's experiments[3] concerning oscillating shock-induced combustion and detonation around a projectile flying into premixed combustible gas, the axisymmetric equations are used. All other results employ the two-dimensional version of equations obtained, as the radial distance y approaches infinity, whereas gradients $\partial/\partial y$ remain finite.

Numerical Method

The governing equations are solved with an unsteady, implicit, cell-centered, structured multiblock, finite volume scheme with an accuracy up to third order in time and space. The conservative variables and the source terms are approximated as constant within a cell of fixed geometry to develop the finite volume formulation for the governing equations. At the same time, the residual vector $\boldsymbol{R}$ is introduced to give

$$V\frac{\partial}{\partial t}\boldsymbol{Q} = -\int_V \left[\frac{\partial}{\partial x}(\boldsymbol{G}_c - \boldsymbol{G}_d) + \frac{1}{y}\frac{\partial}{\partial y}y(\boldsymbol{H}_c - \boldsymbol{H}_d)\right] \mathrm{d}V + V\boldsymbol{S} = -\boldsymbol{R} \tag{10}$$

where the volume integration of the fluxes can be replaced by a surface integration using the Gauss identity.

Spatial Discretization

Roe flux-difference splitting in combination with various total variation diminishing (TVD) limiters was used to discretize inviscid fluxes. TVD techniques allowing up to third-order spatial accuracy were implemented as described by Yee et al.[9] With the convective flux through a cell face defined according to $\boldsymbol{F}_c = \Delta y\boldsymbol{G}_c - \Delta x\boldsymbol{H}_c$, the numerical flux through the cell face is given by

$$\tilde{\boldsymbol{F}}_{c,i+\frac{1}{2}} = \tfrac{1}{2}(\boldsymbol{F}_{c,i} + \boldsymbol{F}_{c,i+1}) + \underline{\boldsymbol{T}}_{i+\frac{1}{2}}\boldsymbol{\Phi}_{i+\frac{1}{2}} \tag{11}$$

with $\underline{\boldsymbol{T}}_{i+1/2}$ as a matrix containing the eigenvectors of the inviscid flux Jacobi matrix $\partial\boldsymbol{F}_c/\partial\boldsymbol{Q}$, evaluated with arithmetic, for example, Roe averaged states, following the procedures outlined by Shuen et al.[10] Yee et al.[9] note that the form of $\boldsymbol{\Phi}_{i+1/2}$ can be divided into spatially second-order symmetric TVD schemes, where the numerical dissipation is independent of the sign of the characteristic speeds, and second-order upwind TVD schemes, where the numerical dissipation is dependent on the sign of the characteristic speeds.

The computations presented in this paper utilize the most efficient and robust symmetric second-order TVD limiter, for which the elements of $\boldsymbol{\Phi}_{i+1/2}$ can be presented as

$$\Phi^l_{i+\frac{1}{2}} = -\psi\left(\lambda^l_{i+\frac{1}{2}}\right)\left[\alpha^l_{i+\frac{1}{2}} - \hat{Q}^l_{i+\frac{1}{2}}\right] \tag{12}$$

with the value $\lambda^l_{i+1/2}$ as eigenvalue of the convective flux Jacobi matrix and ψ as the entropy correction function to λ. The eigenvalues have to be calculated based on averaged variables as the eigenvector matrices. The absolute values of the eigenvalues are increased by the entropy satisfying function ψ if they are too small:

$$\psi(\lambda_i) = \begin{cases} \left(\lambda_i^2 + \tilde{\epsilon}^2\right)\big/2\tilde{\epsilon} & \text{for} \quad |\lambda_i| < \tilde{\epsilon} \\ |\lambda_i| & \text{otherwise} \end{cases} \tag{13}$$

where $\tilde{\epsilon}$ is calculated according to

$$\tilde{\epsilon} = \epsilon(|u\Delta y^0| + |v\Delta x^0| + a)\Delta s \tag{14}$$

According to Yee et al.,[9] the parameter ϵ can be set to zero for weak unsteady shocks and has to be selected carefully, especially for strong steady shocks close to stagnation points. The entropy fix must be applied especially for flows around blunt bodies, to avoid nonphysical solutions displaying the so-called carbuncle phenomenon. The elements $\alpha^l_{i+1/2}$ are defined as

$$\boldsymbol{\alpha}_{i+\frac{1}{2}} = \underline{\boldsymbol{T}}^{-1}_{i+\frac{1}{2}}(\boldsymbol{Q}_{i+1} - \boldsymbol{Q}_i) \tag{15}$$

and the limiter function $\hat{Q}^l_{i+1/2}$

$$\hat{Q}^l_{i+\frac{1}{2}} = \operatorname{minmod}\left(\alpha^l_{i-\frac{1}{2}}, \alpha^l_{i+\frac{1}{2}}\right) + \operatorname{minmod}\left(\alpha^l_{i+\frac{1}{2}}, \alpha^l_{i+\frac{3}{2}}\right) - \alpha^l_{i+\frac{1}{2}} \tag{16}$$

With the use of more compressive, better resolving limiters, in general, their robustness declines.

The viscous fluxes were implemented by central differences, reflecting their physical property.

Temporal Discretization

Instead of directly integrating the system of equations in the time domain, for each physical time step a steady-state problem was solved in a pseudo time domain. For this, a new residual $\boldsymbol{R}^*$ is introduced according to

$$\boldsymbol{R}^* = V\frac{\partial}{\partial t}\boldsymbol{Q} + \boldsymbol{R}(\boldsymbol{Q}) \tag{17}$$

Hence, the problem

$$\boldsymbol{R}^*\left(\boldsymbol{Q}\left[t_i, t^*\right]\right) = \boldsymbol{0}, \qquad t^* \to \infty \tag{18}$$

was solved for an intermediate, physical time level t_i, marching the solution forward in pseudotime t^*. Third-order accuracy in time for nonconstant time steps is achieved when the temporal derivative is expressed in terms of

$$\left.\frac{\partial Q}{\partial t}\right|^{n+1} = (c_1+c_2+c_3)\Delta Q^{n+1} + (c_2+c_3)\Delta Q^n + c_3\Delta Q^{n-1} + O(\Delta t^3) \tag{19}$$

with

$$c_1 = \frac{(\Delta t^{n+1} + \Delta t^n)(\Delta t^{n+1} + \Delta t^n + \Delta t^{n-1})}{\Delta t^{n+1}\Delta t^n(\Delta t^n + \Delta t^{n-1})}$$

$$c_2 = -\frac{\Delta t^{n+1}(\Delta t^{n+1} + \Delta t^n + \Delta t^{n-1})}{\Delta t^n\Delta t^{n-1}(\Delta t^{n+1} + \Delta t^n)}$$

$$c_3 = \frac{\Delta t^{n+1}(\Delta t^{n+1} + \Delta t^n)}{\Delta t^{n-1}(\Delta t^n + \Delta t^{n-1})(\Delta t^{n+1} + \Delta t^n + \Delta t^{n-1})}$$

For a physical time step, the iteration scheme

$$\left[\frac{1}{\Delta t^*}\underline{\boldsymbol{I}} + \left.\frac{\partial \boldsymbol{R}^*}{\partial \boldsymbol{Q}}\right|^m\right]\Delta\boldsymbol{Q}^{m+1} = -\boldsymbol{R}^*|^m \tag{20}$$

with m as the subiteration count, has to be applied until the residual in the pseudo time domain $\boldsymbol{R}^*$ vanishes. This approach has been used by Choi et al.[11] for their time-accurate calculation of oscillating shock-induced combustion, with up to second-order accuracy in time.

Lower-Upper Symmetric Gauss–Seidel Scheme

In Eq. (20), the Jacobi matrices corresponding to the right-hand side $\boldsymbol{R}^*$ are included in the left-hand side by $\partial\boldsymbol{R}^*/\partial\boldsymbol{Q}$. For

a mathematically complete left-hand-side formulation, Jacobi matrices for the chemical source term, the inviscid fluxes, the viscous fluxes, and the source term due to axisymmetry would have to be computed. In this work, all Jacobi matrices but the axisymmetric one are included in the left-hand side. The components of these matrices are given by Shuen,[12] who also provides a Jacobi matrix for the thin-shear-layer approximated viscous fluxes. The resulting system of equations is then solved by the lower–upper symmetric Gauss–Seidel scheme, originally proposed by Jameson and Turkel.[13]

For a time-accurate integration, a suitable time step must be found locally for each cell, and then the minimum local time step must be used globally. Even for a steady-state calculation, a finite time step is beneficial because the factorization error reduces the stability of the implicit method. The time-step calculation requires the knowledge of the convective and diffusive spectral radii, Λ_c and Λ_d, based on the eigenvalues of the inviscid and viscous Jacobi matrices and the local cell metrics. Details of the calculation of the spectral radii and eigenvalues of the flux matrices can be found in Refs. 14 and 15. The local time step is then calculated according to the following equation, which contains the Courant–Friedrichs–Lewy (CFL) number:

$$\Delta t = \mathrm{CFL}/\Lambda_t = \mathrm{CFL}/(\Lambda_c + \Lambda_d) \tag{21}$$

In the case of a fully implicit left-hand side and an integration in time employing subiterations, only the inviscid time-step restrictions need to be applied. Otherwise, especially at the startup of the computation, for more complex flows the viscous time-step restriction was required as well to ensure solution stability.

With a suitable time step calculated, the time-marching integration can proceed, and its convergence progress is monitored by the calculation of the residual. Here, a reference state is required to normalize the change of conserved variables. An obvious choice for such a reference state would be the inflow conditions, according to

$$\boldsymbol{Q}_{\mathrm{ref}} = [\rho_\infty,\ \rho_\infty U_\infty,\ \rho_\infty U_\infty,\ \rho_\infty E_\infty,\ \rho_\infty, \ldots,\ \rho_\infty] \tag{22}$$

The residual for a cell is then calculated by applying the L_2-norm to the change of the conserved variables that was divided by the reference state and the local time step. The division by the local time step does not apply for a pure Newton-type iteration, where the time step tends to infinity:

$$\varepsilon_{\mathrm{cell}} = \frac{1}{\Delta t} \cdot \left[\left(\frac{\Delta \rho}{\rho_\infty} \right)^2 + \left(\frac{\Delta(\rho u)}{\rho_\infty U_\infty} \right)^2 + \left(\frac{\Delta(\rho v)}{\rho_\infty U_\infty} \right)^2 + \left(\frac{\Delta(\rho E)}{\rho_\infty E_\infty} \right)^2 + \sum_{i=1}^{N_s - 1} \left(\frac{\Delta(\rho Y_i)}{\rho_\infty} \right)^2 \right]^{\frac{1}{2}} \tag{23}$$

The overall residual ε is then obtained by averaging the residual obtained for all cells,

$$\varepsilon = \frac{1}{N_{\mathrm{cells}}} \cdot \sum_{N_{\mathrm{cells}}} \varepsilon_{\mathrm{cell}} \tag{24}$$

This method of calculating the residual was applied to the results of the iteration scheme and those of the subiteration scheme.

Validation

Oscillating Shock-Induced Combustion Around Projectile

When an axisymmetric projectile is fired into a combustible gas mixture, oscillating shock-induced combustion can occur under certain circumstances. Lehr[3] performed extensive experiments to examine this phenomenon, and his findings are widely used for the validation of numerical methods for reactive flow computations.

Therefore, the present code was used to reproduce the flowfield for a projectile flying into the gas mixture at a Mach number of 4.48. The initial pressure and temperature are 43,383 Pa and 292 K; air is mixed with hydrogen stoichiometrically.

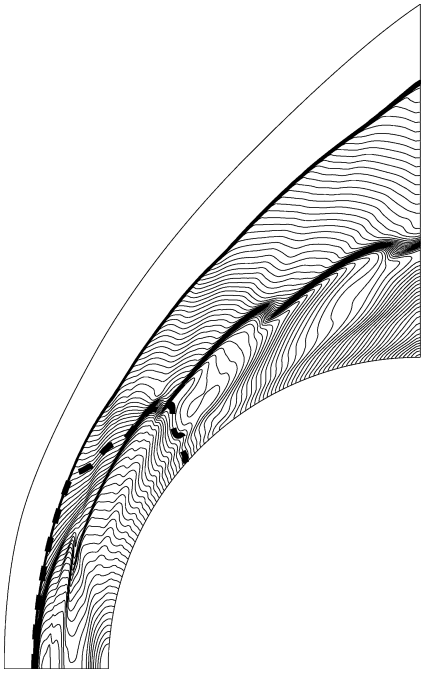

a) Projectile Mach number 4.48

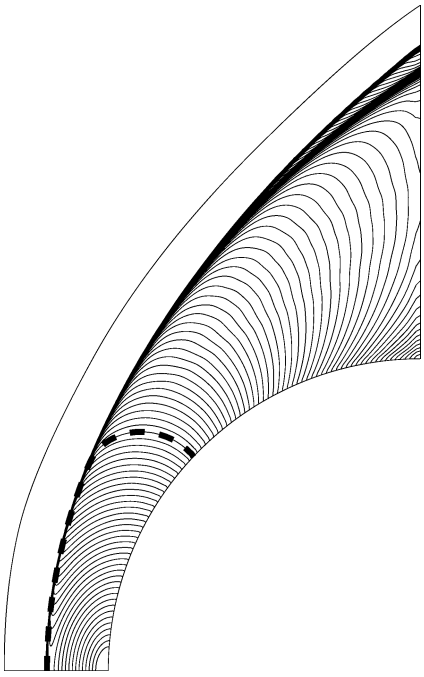

b) Projectile Mach number 6.46

Fig. 2 Instantaneous Mach number contours for shock-induced combustion and detonation around an axisymmetric projectile with flow Mach numbers a) $M = 4.48$ and b) $M = 6.46$; contour level represents a change in Mach number of 0.025 and - - - -, local Mach number of 1.

As pointed out by Choi et al.,[11] viscous effects are of minor importance in this experiment. Hence, the inviscid, axisymmetric equations for a reactive multispecies gas are used. The gas is represented by 9 species, with nitrogen assumed inert, and the reaction mechanism is represented by 19 elementary reaction equations, as suggested by Choi et al.[11] The numerical setup was chosen to equal the baseline method presented by Choi et al.,[11] and the calculations were performed using a mesh with 300 cells in the direction normal and 200 cells tangential to the projectile surface.

Instantaneous Mach number contours clearly show the complex flame front behind the leading bow shock in Fig. 2a. The oscillation frequency obtained from calculations with the present code was

427 kHz, which compares well with the 425 kHz measured in the experiment and also reproduced numerically by Choi et al.,[11] and that results in a relative error in frequency below 0.5%. With this frequency, the time accuracy in combination with inviscid flow and a complex chemical reaction scheme is validated.

Detonation Around Projectile

With all parameters of the preceding validation case kept the same and the Mach number of the projectile increased to 6.46, the oscillating shock-induced combustion is replaced by a detonation wave, where the shock wave and the reaction zone merge.

At a radial distance far enough from the projectile axis, the detonation wave bifurcates into a shock wave and a flame front. This phenomenon, recorded in Lehr's experiments,[3] is reproduced well numerically and shown in Fig. 2b. Both steady-state and time-accurate calculations produce the same result for this case.

The standoff distance of the detonation wave in the experiment is 1.5 mm, which equals that of the numerical result. At a streamwise position where the rounded projectile surface merges into the straight part, which is equivalent with the outflow boundary of the domain used for the computation, the flame front is located at a radial distance of 12.8 mm and the shock wave at a radial distance of 13.9 mm in the experiment. The computation overpredicts these distances at 14.1 and 15.1 mm, resulting in relative errors of 10 and 9%, respectively. Note that the measurement of distances in the schlieren photograph of the projectile is subject to some error because the projectile flies at a slight angle relative to the flight path required by the schlieren system. The exact position of the bifurcation of the detonation wave into shock wave and flame front is difficult to locate, especially in the case of the schlieren photograph of the experiment. In the case of the numerical result, the position is approximately 2.5 mm downstream from the projectile nose and 10 mm away in radial direction from the projectile axis.

With these results, the present numerical method is validated against flows containing oscillating shock-induced combustion as well as detonation waves.

Flow over Flat Plate

A further important function of the flow solver is the correct calculation of viscous effects. Ideally, such a validation should be made against experimental results of a reactive boundary layer at supersonic velocities or similar flow. However, due to the lack of availability of such experimental data, only a simpler, nonreactive case is considered here because the chemical reaction scheme and its coupling with the inviscid components of the flow solver are demonstrated in the preceding subsections. Hence, the flow of air over a flat plate at fixed temperature was examined to compute the boundary layer and its temperature profile. The temperature along the flat plate of a length of 1 m was kept the same as that of the inflow.

The inflow Mach number, pressure, and temperature are 2, 2566 Pa and 221.6 K, respectively. The incoming air gas flow was simulated by a two-species gas mixture containing oxygen and nitrogen of molar fractions of $X_{O_2} = 0.235$ and $X_{N_2} = 0.765$. Supersonic inflow and outflow boundary conditions were imposed. In the case of the outflow boundary, this is not entirely correct because of the upstream influence of subsonic flow. However, with the pressure across the boundary layer approximately constant, the pressure from the outer, supersonic flow at the outflow boundary can be prescribed for the subsonic outflow regions within the boundary layer.

The temperature profile at a streamwise position of $x = 0.915$ m is shown in Fig. 3, where it is compared to numerical values obtained by Lawrence et al.[16] A good agreement was found despite the species properties in the present code being calculated by means of kinetic gas theory instead of Sutherland's law. Also, the representation of air as a mixture of oxygen and nitrogen does not degrade the solution quality.

Another case involving viscous effects, a diffusive mixing problem, is presented by Ess,[14] where the correct implementation of the species diffusion is validated. This case is only noted here because the study presented in the remaining text assumes stoichiometrically premixed hydrogen–air gas flow, where the molecular diffusion is of less importance, as in the mixing of different species with initially high gradients of species concentration between layers of different species.

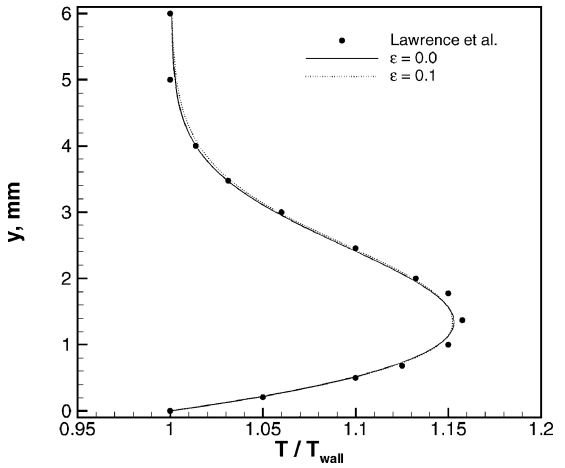

Fig. 3 Temperature profile for supersonic flow over flat plate calculated with different entropy correction coefficient ϵ. [See Eqs. (13) and (14).]

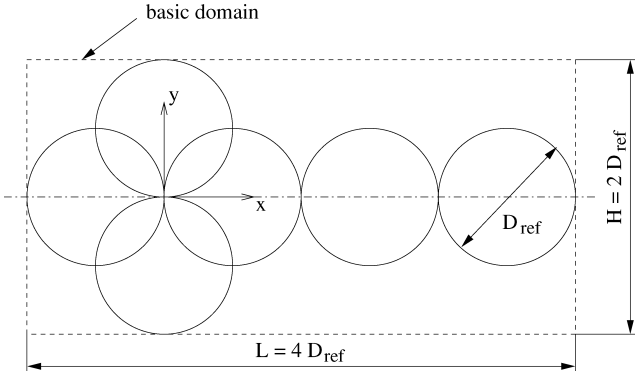

a) Domain dimensions in multiples of reference diameter

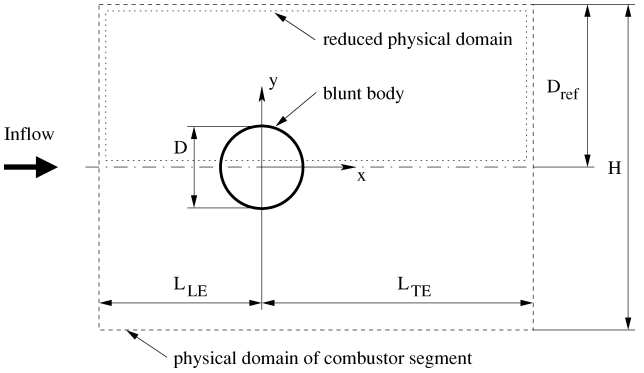

b) Definition of reduced physical domain

Fig. 4 Geometrical setup for parameter study; boundary conditions imposed are supersonic inflow and outflow at the vertical boundaries, symmetry plane through the center of the blunt body, and either a symmetry plane or solid wall as outer horizontal boundaries: wall temperatures, blunt body, and horizontal solid wall are kept constant and equal that of inflow.

Blunt-Body Generated Combustion

Problem Definition

The physical domain was set up as a rectangular flow channel in multiples of a reference diameter with inflow direction as shown in Fig. 4. The geometrical dimensions were selected so that the

blunt-body diameters are of an order comparable to the projectile diameters used in Lehr's experiments.[3] The channel height is $H = 0.06$ m and, hence, yields a reference diameter $D_{\text{ref}} = 0.03$ m. The channel blockage ratio (CBR) is defined as the ratio of blunt-body diameter D over channel height H. For all cases presented in the following text, the channel height was kept constant and the blunt-body diameter changed to yield the desired CBR.

Because the rod center is placed at one-half of the channel height normal to the flow direction, symmetry conditions can be applied to reduce the size of the domain to one-half of that of the original domain. In this study, the lower boundary of the reduced domain is always a symmetry plane, whereas the upper boundary is either a symmetry plane or a solid wall at constant temperature. Supersonic inflow and outflow are imposed as vertical boundary conditions.

Typical hypersonic flight conditions for a scramjet powered vehicle are assumed as follows[17]: flight altitude 38 km and flight Mach number in excess of 10. Previous studies for shock or detonation-induced combustion ramjets then allow an estimate for the combustor inflow conditions. Because the exact design of the engine inlet, which involves problems of efficient air–fuel mixing and premature ignition, is not part of this work, a simplified, uniform inflow is prescribed.

It was assumed that the inlet raises the static pressure at the entrance of the combustor to 10,000 Pa and the inflow temperature to 700 K and reduces the inflow Mach number to 5. Species mass fractions are chosen to resemble a stoichiometrically premixed air–hydrogen gas flow. The wall temperatures were set to equal the inflow temperature at 700 K.

The chemical reaction scheme employed uses 13 species and 33 partial reaction mechanisms, as proposed by Jachimowski.[18] This scheme is widely used for the numerical analysis of supersonic reactive flows characteristic of scramjet applications.

The Reynolds number based on the reference diameter is $Re = 1.23 \times 10^5$. Hence, for a realistic design study, turbulence must be taken into consideration. Some aspects of turbulence for hypersonic flows are discussed by Anderson[19] and the accurate modeling, especially of reactive flows, is far from being well understood. Choi et al.[20] simulate the flow around a ram accelerator in an expansion tube with air–hydrogen gas. The flow Mach number is 5.2 and the Reynolds number based on the combustor length is 10^6. Despite the higher Reynolds number in their study, Choi et al. do not see any clear evidence of the importance of turbulence on the global combustion charactersitics in the corresponding experiment. Furthermore, they state that there is no adequate turbulence model to predict the interaction between chemistry and turbulence in the region of strong shock wave/boundary-layer interactions. Because at this stage the basic phenomena of the configuration proposed were examined, the flow was assumed laminar to reduce computational cost.

Computational Aspects

The steady-state computations were performed on a parallel computer using up to 66 processors with a spatial accuracy of second order. The fully implicit time-marching scheme, with a source term and inviscid and viscous flux Jacobi matrices, was used for these computations with three subiterations. To improve convergence, the local time step based on a CFL number of 5 was used. Hence, the third-order accuracy of temporal integration due to the subiterations did not maintain time accuracy, but provided a better subiteration convergence.

The subiterations were employed to compensate for the explicit coupling between the subdomains introduced by the subdivision of the domain for the efficient parallel computations and, generally, result in an excellent convergence. Parallel computation with subiterations allowed the exclusive application of the purely convective flux-based time-step calculation, yielding significantly larger time steps in the first stage of the computation.

The time-accurate calculations follow the same pattern, with the exception that the same time step was used everywhere in the domain to preserve the time accuracy. Also, the time step was reduced corresponding to a CFL number of 2.5, to obtain increased accuracy. Different numerical setups were considered, for example, second-order temporal accuracy with a CFL number of 1.0 and five subiterations and third-order temporal accuracy with a CFL number of 2.5, utilizing three and five subiterations. For all time-accurate calculations without outflow boundary condition related stability problems, all of the setups just introduced worked, with the exception of the case with a CBR of 1/3 for the domain with a length of five reference diameters. In this particular case, at least five subiterations were required for a stable and accurate result. Details will be discussed hereafter.

For the standard steady-state computation, the domain was initialized with freestream conditions. This produces a rarefaction wave close to escape velocity behind the blunt body and a strong shock wave moving upstream from the blunt body until the final position is reached. Hence, an entropy correction coefficient of $\epsilon = 0.5$, which is in the upper range suggested in the literature,[9] was applied to avoid nonphysical solutions. Additionally, the time step must be restricted at the start of the calculation before it slowly increases up to the regular value.

For the time-accurate simulation, the domain was initialized with the same properties (density, pressure, and gas composition) as the inflow, but the velocity set to zero. This assumes that before the operation of the combustor the outside pressure and temperature reside in the duct. At the beginning of the operation, the combustor is then opened instantaneously and the flow develops thereafter. However, the proper initial setup of the combustion chamber cannot be determined without exactly knowing how the entire engine is designed.

Grid Convergence Study

A grid convergence study was performed for the CBR = 1/6 with a symmetry plane as the upper, horizontal boundary of the domain. This CBR was selected for a grid convergence study because it does not produce any unsteady flow behavior, which would require an excessively expensive time-accurate calculation of the resulting flow on refined meshes. At the same time, the case with this channel blockage contains a more complex shock and combustion wave structure representative for the types of flow examined.

The study employs four different meshes with the number of cells varying from 22,500 for the coarse mesh, 44,900 for the regular mesh; 90,000 for the fine mesh; and 179,600 for the finest mesh. The fine mesh was created based on the coarse mesh by doubling the number of cells in each block in each direction.

The details of multiblock arrangement, grid blocks, as well as details of the regular mesh are presented in Fig. 5. For all cases considered, the boundary layers along the blunt body and the upper wall, where relevant, are well resolved. For the grid system presented with CBR = 1/6, the radial spacing of the first cell is 3.5×10^{-6} m, increasing by a factor of 1.19 away from the blunt body. For varying sizes of blunt bodies, the radial spacing of the first cell is scaled linearly with their diameter. At the streamwise position of $x = 0$ m, this yields a normalized wall distance of $y^+ = 1.5$ and a boundary layer resolved with 20 cells. For cases with a solid wall as an upper boundary of the domain, the cell clustering along the wall is similar, resolving the boundary layer one-half a reference diameter downstream from the inflow boundary at $x = 0.015$ m with 25 cells. The maximum normalized wall distance along the upper wall is $y^+ = 0.5$, which is refined compared to the clustering around the blunt body to resolve possible flow separation at bow shock reflection well. This location is slightly upstream before the recirculation and combustion zone produced by the bow shock reflection at the wall for a channel bloackage of 1/6. Details of the recirculation zone will be discussed hereafter.

The convergence histories of the parallel computations with three subiterations for each iteration step and a standard numerical setup are given in Fig. 6. The Mach number along the upper symmetry boundary and distribution over the entire domain for the different cases are shown in Fig. 7. As the grid is refined, the shock waves become better resolved, which can be seen by the thicknesses of the shock reflection at the symmetry plane at the upper boundary of the domain: They are 2.024×10^{-3} m, 1.256×10^{-3} m, 0.880×10^{-3} m, and 0.600×10^{-3} m, for meshes employing 0.5, 1, 2, and 4 times the

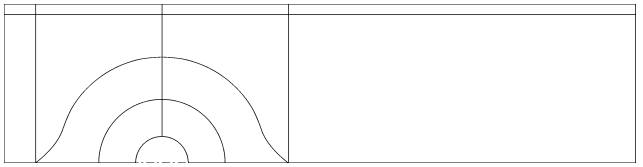

a) Multiblock arrangement

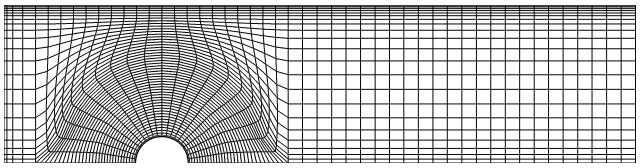

b) Every fifth grid line of mesh for CBR = 1/6

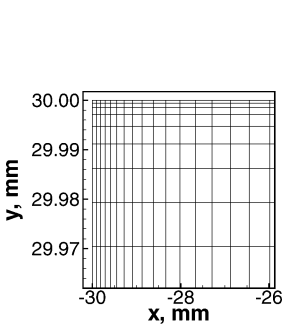

c) Mesh at inflow boundary

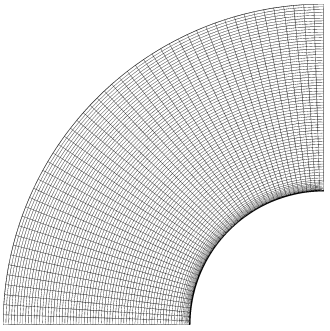

d) Mesh around blunt body

Fig. 5 Grid system for grid convergence and parameter study.

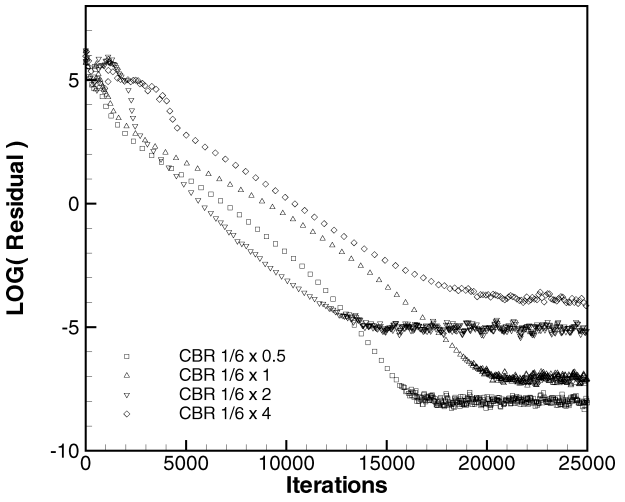

Fig. 6 Convergence histories [Eq. (24)] for grid convergence study employing different meshes: The mesh ×0.5 contains 22,500 cells; the mesh ×1 contains 44,900 cells; the mesh ×2 contains 90,000 cells; and the mesh ×4 contains 179,600 cells.

number of cells of the regular mesh. The changes in shock thickness from coarse to refined grid levels are decaying according to 7.676×10^{-4} m, 3.771×10^{-4} m, and 2.792×10^{-4} m, with ratios of thickness from finer to coarser levels from 1.611 and 1.427 to 1.466, whereas the ratio of numbers of cells in one geometrical direction from a finer to a coarser mesh is 1.414. Hence, apart from the coarsest to the regular mesh, the shock thickness reduces at the same ratio at which the mesh is refined within an error of below 4%.

Parameter Study for Channel Blockage

For the two configurations with a symmetry plane or a solid wall as boundary condition for the upper boundary of the computational domain, a parameter study was performed to examine the influence of different channel blockages. The CBRs considered were

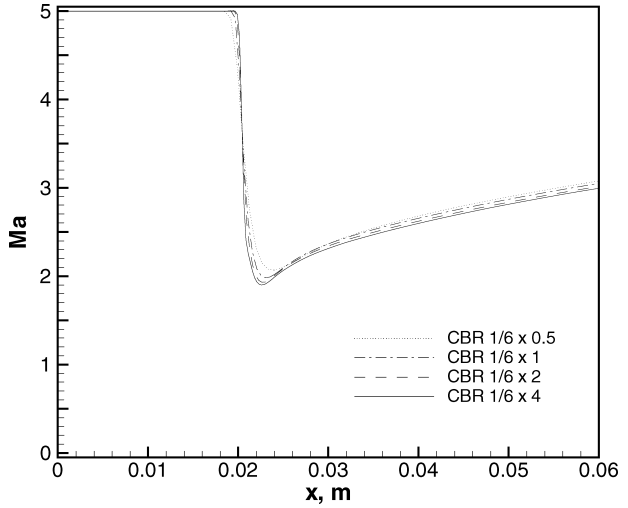

a) Mach number distribution at upper symmetry plane

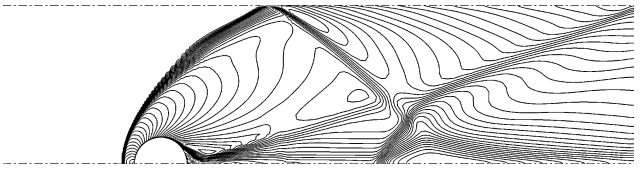

b) Coarse mesh, 22,500 cells

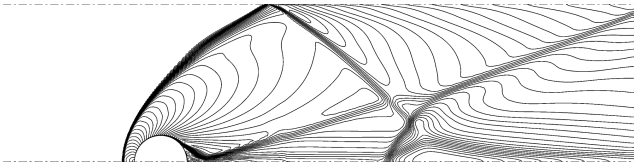

c) Standard mesh, 44,900 cells

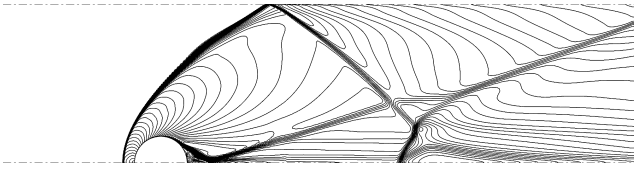

d) Fine mesh, 90,000 cells

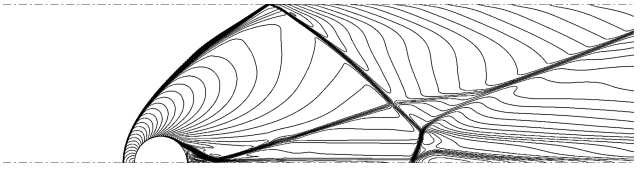

e) Finest mesh, 179,600 cells

Fig. 7 Mach number distributions for different mesh systems; Mach number contour corresponds to Mach number change of 0.1.

CBR = 1/18, 1/12, 1/9, 1/6, 1/4, and 1/3. Initially, for all cases, steady-state calculations were performed on the standard mesh, before specific ones were computed time accurately.

Double Symmetry Plane

The convergence histories for the steady-state calculations of cases with a symmetry plane as upper domain boundary are given in Fig. 8. Excellent convergence could be achieved for all CBRs, except for CBR = 1/3. This particular case will be discussed in detail following the presentation of the steady-state results.

The Mach number and hydroxyl mass fraction contours are shown in Fig. 9. The basic components of the flowfield are a leading bow shock originating in front and a tail shock originating behind the blunt body. With increasing blunt-body diameter, the shock angles rise and the bow shock reflection point on the symmetry plane at the

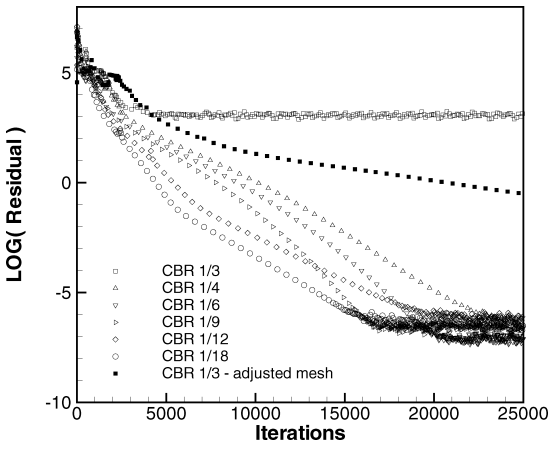

Fig. 8 Convergence histories [Eq. (24)] for different CBRs with symmetry plane as upper domain boundary; standard mesh (×1) is used.

upper boundary of the domain moves upstream. For all CBRs up to 1/4, the leading bow shock reflection at the upper domain boundary is a regular reflection; for 1/3, it becomes a Mach stem reflection. As shown in Figs. 9e and 9g, for channel blockages of 1/9 and 1/6, the following reflection of the bow shock wave at the symmetry plane of the lower boundary of the domain produces a complex flow structure. For further increased CBRs of 1/4 and 1/3, the bow shock wave reflected at the upper symmetry plane meets with the recirculation zone behind the blunt body, as shown in Figs. 9i and 9k. For the CBR of 1/3, the tail shock wave is being reflected at the upper domain boundary within the given domain length.

An important aspect is the distinction between shock and detonation induced combustion. Following the method of Kasahara et al.,[4] it is common practice in experimental detonation research to use the OH-radical self-emmision images in combination with schlieren photographs of the flow to determine the regime of combustion. If the hydroxyl self-emmision photograph matches the position of a wave in the corresponding schlieren photograph, the wave can be identified as a detonation wave. Hence, to find qualitatively

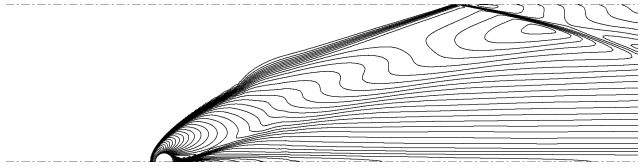

a) CBR = 1/18

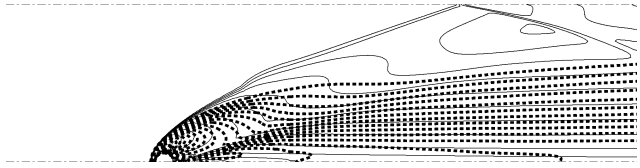

b) CBR = 1/18

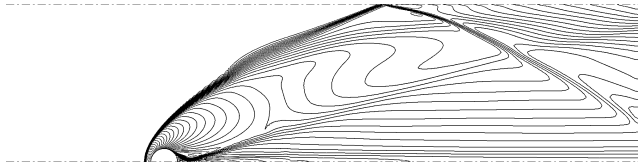

c) CBR = 1/12

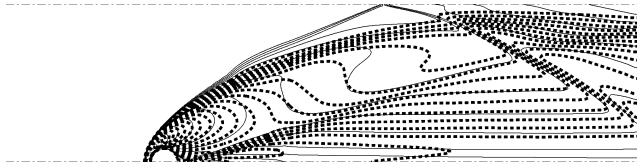

d) CBR = 1/12

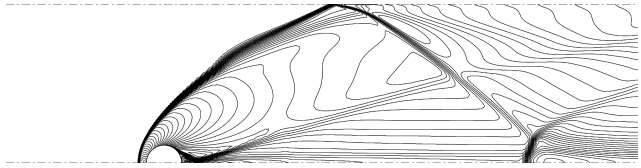

e) CBR = 1/9

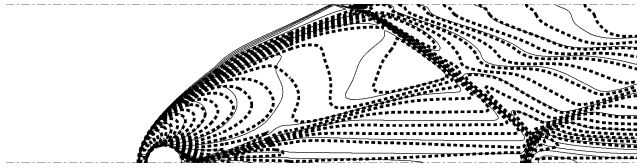

f) CBR = 1/9

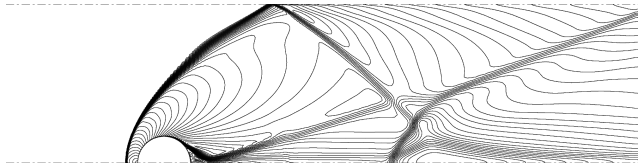

g) CBR = 1/6

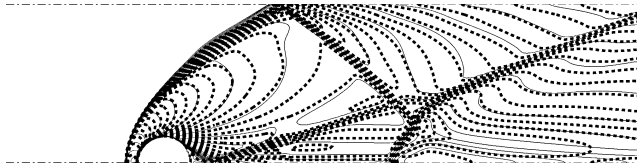

h) CBR = 1/6

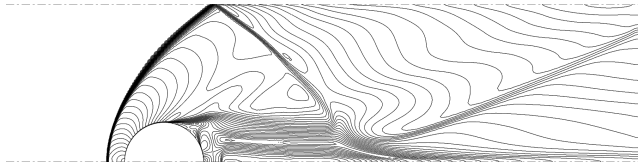

i) CBR = 1/4

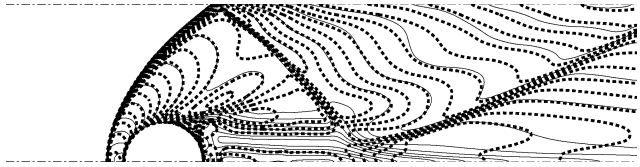

j) CBR = 1/4

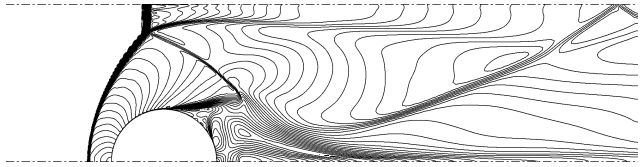

k) CBR = 1/3

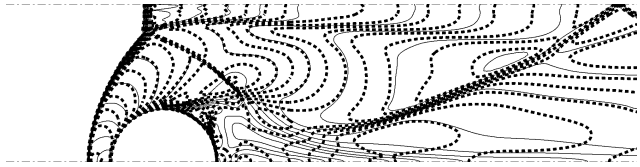

l) CBR = 1/3

Fig. 9 Mach number contours for different CBRs with symmetry plane as upper domain boundary to the left (contour level represents step of $\Delta M = 0.1$); Mach number and OH mass fraction contours for different CBRs with wall as upper domain boundary to the right: ——, Mach number contours with $\Delta M = 0.25$ for each level and - - - -, hydroxyl contours with ΔY (OH) = 0.002 for each level.

the extent of shock-induced combustion, hydroxyl contours are superimposed on Mach number contours. As the channel blockage increases, the extent of shock-induced combustion decreases. For a CBR of 1/4 and above, the entire combustion is due to detonation.

It was mentioned that for the CBR of 1/3 the solution did not converge. Therefore, this particular case was also calculated time accurately, resulting in the identical flowfield as that observed for the steady-state calculation. A close examination of the flow reveals that the cause for the convergence problem lies in small perturbations along the Mach stem reflection of the bow shock wave. On a mesh with the number of cells around the blunt body doubled and that along the upper symmetry plane normal to the wall slightly reduced, a second set of both the steady-state and time-accurate calculations produced a converged result without any perturbations. Hence, the instabilities are demonstrated to be of numerical nature and the resulting flowfield to be steady and stable.

The temperature, water, hydrogen, and hydroxyl mass fractions at the exit plane of the domain are compared in Fig. 10 for CBR = 1/3, 1/9, and 1/18. For the smallest channel blockage of 1/18, there is no significant combustion for the upper 15% of the domain, whereas for the largest CBR of 1/3 the temperature levels are, in general, higher than for the CBR of 1/9. This increased temperature yields a reduction in water mass fraction over most of the exit plane and an increase in hydroxyl mass fraction.

Symmetry Plane and Solid Wall

In the second configuration, the symmetry plane at the upper boundary of the domain is replaced with a solid wall at constant

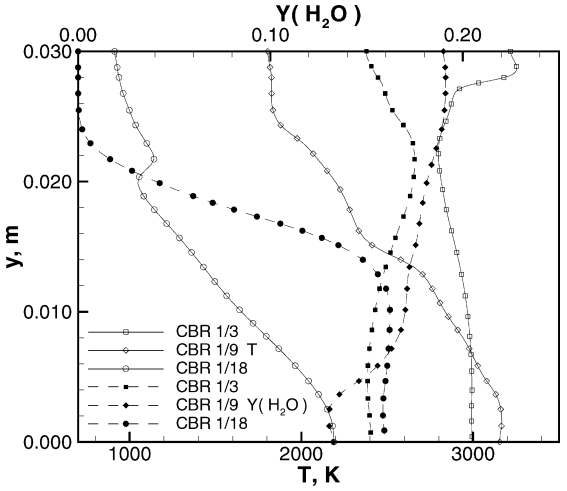

a) Temperature and water mass fraction

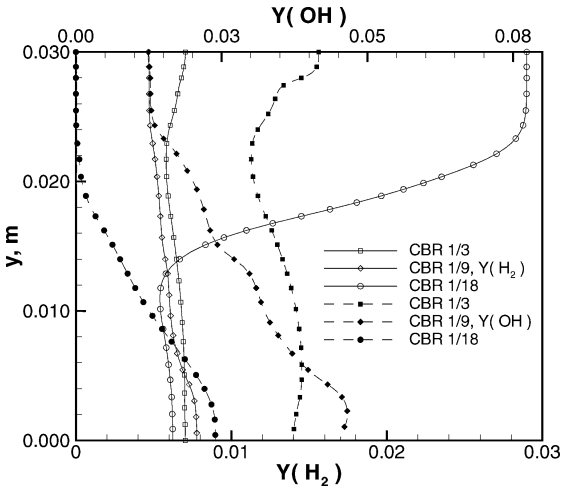

b) Hydrogen and hydroxyl mass fractions

Fig. 10 Temperature and water, hydrogen and hydroxyl mass fraction distribution along outflow boundary for different CBRs and symmetry plane as upper boundary.

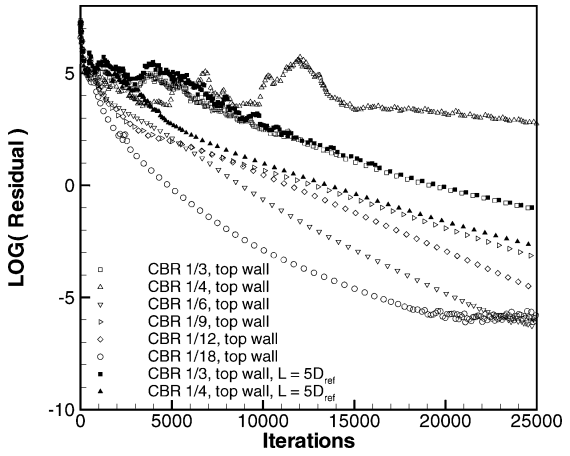

Fig. 11 Convergence histories [Eq. (24)] for different CBRs with solid wall as upper domain boundary; standard mesh (×1) is used.

temperature. The convergence histories for the steady-state calculations of these cases are given in Fig. 11. The configuration with upper solid wall yields convergence problems for CBR = 1/4 and less rapid convergence for CBR = 1/3 when compared to the remaining cases. Both cases are calculated time accurately, and results are discussed after the presentation of the results for the steady-state calculations. All cases apart from that with CBR = 1/4 are shown as steady-state results for a domain with a length of four reference diameters.

Mach number and hydroxyl mass fraction contours for the resulting flowfields are given in Fig. 12. The start of the boundary layer causes a weak, oblique shock wave originating at the upper edge of the inflow boundary. With increasing length, the boundary layer thickens, and, especially in front of the bow shock reflection point, a complicated flow structure results, as shown in Fig. 12g. For the largest channel blockage shown in Fig. 12i, flow with a detonation wave standing normal in front of the blunt body results.

The hydroxyl mass fraction contours shown for the configuration with the upper wall are, again, used to identify the regions where combustion starts. For the smallest channel blockage ratio of 1/18, the situation is very similar to that of the configuration with the symmetry plane because the resulting combustion zone does not cover the entire height of the domain. Interestingly, for this channel blockage there is not even a combustion zone along the upper wall, as shown in Fig. 12b. However, increasing the channel blockage ratio to 1/12 produces this additional combustion zone along the upper wall, as can be seen in Fig. 12d. The combination of boundary layer along the upper wall and the bow shock reflection produce an additional combustion zone ahead of the bow shock reflection point, shown in Figs. 12f and 12h, which increases in size as the channel blockage rises.

Up to the CBR of 1/9, there are significant parts of shock-induced combustion along the bow shock. Also, the recirculation zone in front of the bow shock reflection point at the upper wall is a region with shock-induced combustion. This is shown best in Fig. 12h, where hydroxyl mass fraction contour lines are limited to the recirculation zone, which is preceeded by an oblique shock too weak to initiate instantaneous combustion.

Details of the flowfield around the blunt body for CBR = 1/6 are shown in Fig. 13 that emphasise the complexity of the resulting flow structure. Figure 13a shows three vortices in the combustion zone preceding the bow shock reflection point, two mathematically positive (anticlockwise) and one negative (clockwise). This combustion zone is preceded by an oblique shock wave, forming a zone of shock-induced combustion, whereas the bow wave in front of the blunt body is a detonation with a locally coupled shock wave and flame front, as indicated in Fig. 13b. For the inflow conditions used in this study, a detonation wave at an angle of 41.8 deg relative to the direction of the inflow corresponds to Chapman–Jouguet conditions. This value can be obtained by considering the flow over a wedge and varying the wedge angle until a minimum detonation wave angle is found. Because the lowest detonation wave angle

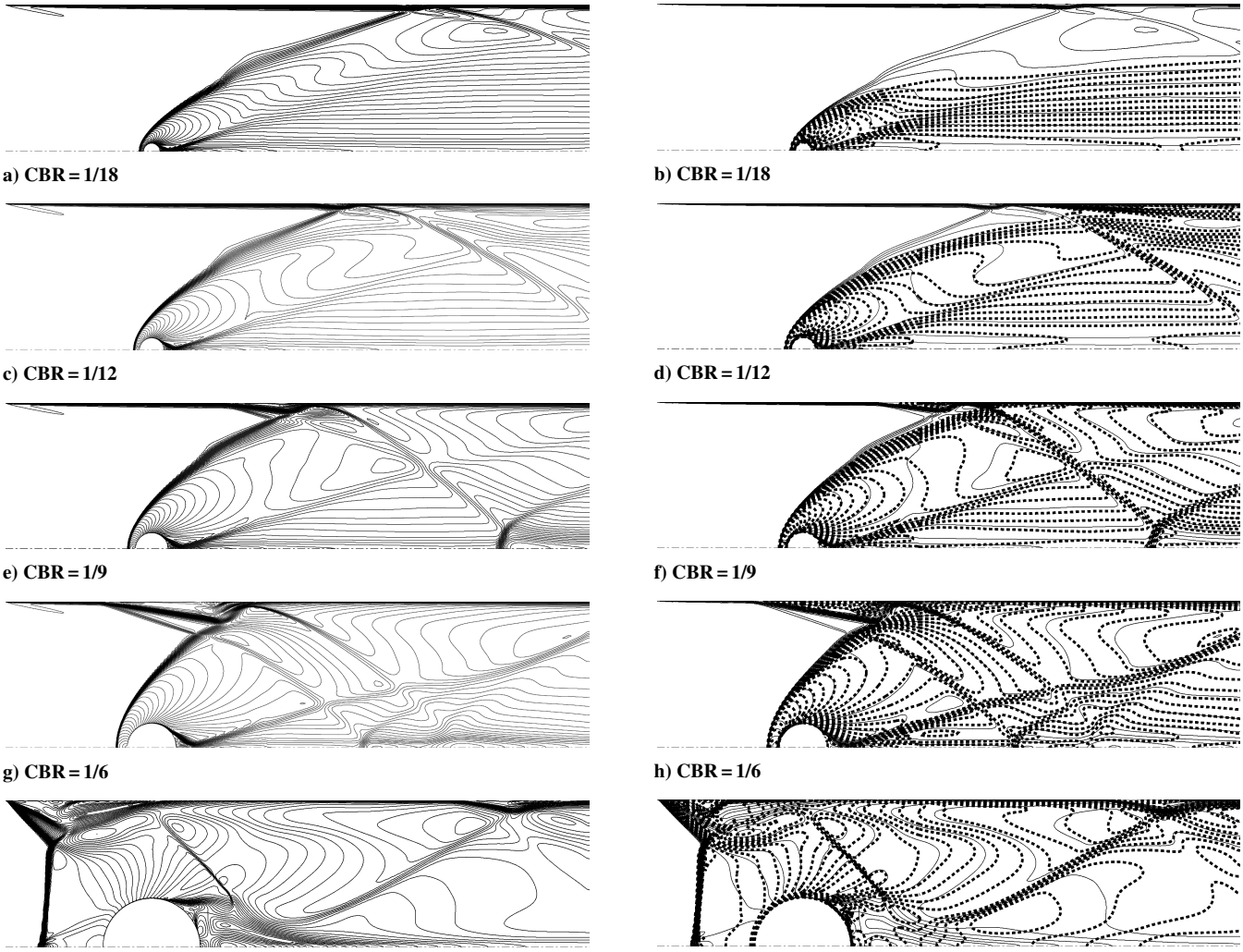

Fig. 12 Mach number contours for different CBRs with wall as upper domain boundary to the left (contour level represents step of $\Delta M = 0.1$); Mach number and OH mass fraction contours for different channel blockage ratios with wall as upper domain boundary to the right: ——, Mach number contours with $\Delta M = 0.25$ for each level and - - - -, hydroxyl contours with $\Delta Y(\mathrm{OH}) = 0.002$ for each level.

found in the particular case shown in Fig. 13b is 46 deg, from the axis of symmetry to the point where the oblique shock wave meets the bow wave, an overdriven, oblique detonation wave is present. For cases with smaller channel blockage or a symmetry plane as an upper boundary of the domain, the detonation wave bifurcates into a shock wave and flame front, resulting in shock-induced combustion. An additional recirculation zone can be found behind the blunt body, with mathematically negative orientation.

To clarify the situation for the cases with less convergence, a time-accurate calculation was performed for CBR = 1/4 and 1/3. A careful analysis revealed that the reason for the convergence problems and the cause of flow instability is the reflection of the tail shock wave at the boundary layer along the solid wall at the upper boundary of the domain, in particular, its proximity to the outflow boundary. Because the physical conditions after the combustor are unknown and dependent on the specific design of the nozzle attached, the outflow boundary is modeled as supersonic outflow, extrapolating values from within the domain. The constellation of the bow shock reflection causing an additional pressure rise, and ultimately boundary-layer separation, in close proximity to the outflow boundary, causes large-scale flow separations. As time progresses the flow reattaches and, for the particular CBR of 1/4, detaches again. This occurs repetitively and, while forming a normal detonation wave in front of the blunt body, the flow is not allowed to settle down and reach a steady-state solution.

In the case of the largest CBR of 1/3, the flow separation process is the same, but less pronounced. Also, after some time a solution is approached that compares well with the preceding result of the steady-state calculation.

To clarify the nature of the flow separation, the simulations were performed for the same channel blockages 1/4 and 1/3, however, utilizing a domain with extended length $L = 5D_{\mathrm{ref}}$. In this extended domain, the tail shock reflection point is well upstream of the outflow boundary, removing the influence of the outflow boundary.

Steady-state calculations for both cases produced converged solutions, with a flowfield comparable to lower channel blockages for CBR = 1/4 and flow with a normal detonation wave standing in front of the blunt body for CBR = 1/3. Time-accurate calculations up to 1 ms were then performed to confirm that the steady-state results are correct and that the resulting flows are indeed stable. The startup process for CBR = 1/4 and 1/3 are shown in Figs. 14 and 15, respectively. Already in the startup process, the formation of a normal detonation wave can be well observed in Fig. 15e.

The long-term solutions for both CBRs shown in Figs. 16 and 17 demonstrate how the steady-state result is approached.

Assessment of Global Parameters

The parameter considered first is the thrust potential, which is defined following that of Riggins et al.[21] as

$$\Delta Th(x) = \frac{1}{\dot{m}} \left\{ \iint\limits_{\Gamma^*(x)} (\rho \boldsymbol{u}^2 + p)^* \cdot \boldsymbol{n} \, \mathrm{d}\Gamma - \iint\limits_{\Gamma^*_{\mathrm{inflow}}} (\rho \boldsymbol{u}^2 + p)^* \cdot \boldsymbol{n} \, \mathrm{d}\Gamma \right\} \tag{25}$$

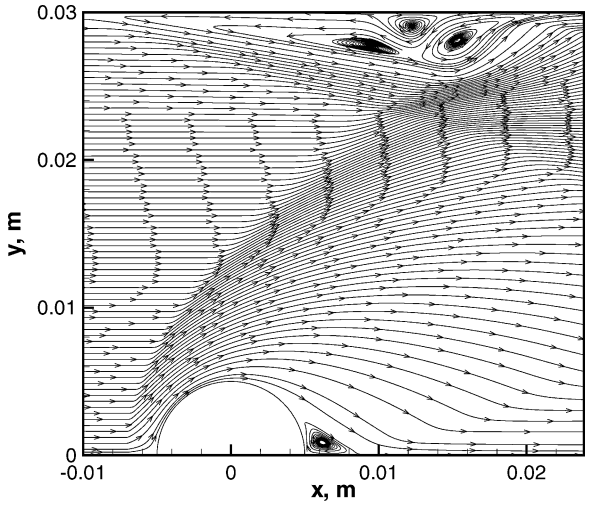

a) Streamtraces

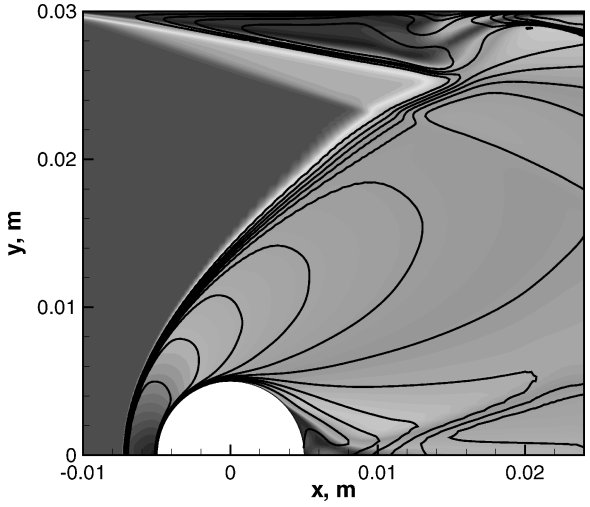

b) Mach number (flood) and hydroxyl (line, $\Delta Y_{OH} = 0.005$) contours

Fig. 13 Flow details for CBR = 1/6 with solid wall as upper boundary.

In the particular cases presented here, only planes normal to the direction of the inflow at locations x downstream from the duct entrance are considered. The properties at the position in the flow are thought to be isentropically expanded, with frozen gas composition for asterisk properties, representing the maximum thrust achievable. The properties of each cell intersected by the plane, for which the thrust potential is calculated, are expanded to the same exit pressure, which is found iteratively, so that the area resulting from the expansions of all cells in that plane matches eight times the duct height.

In Fig. 18a, the thrust potential along the duct is shown for selected CBRs. For cases with a solid wall as an upper boundary of the domain, a small reduction of thrust potential due to friction losses can be observed from the beginning, whereas those with a symmetry plane instead of the solid wall show first losses as the bow shock in front of the blunt body is reached. For the channel blockage of 1/6 the additional wall adds 5% drag compared to the setup with a symmetry plane, where the amount of drag added is roughly the same for the cases with subsequently smaller channel blockages. After the initial reduction of thrust potential, the heat release due to chemical reaction increases the thrust potential again. However, in the case of a channel blockage of 1/3 and the domain with a length of five reference diameters, the losses due to the normal detonation wave in front of the blunt body are so large that the heat release is insufficient to achieve a positive thrust potential at the domain exit. Furthermore, the heat release itself is reduced due to the high levels of temperature after the normal detonation wave, as will be shown hereafter.

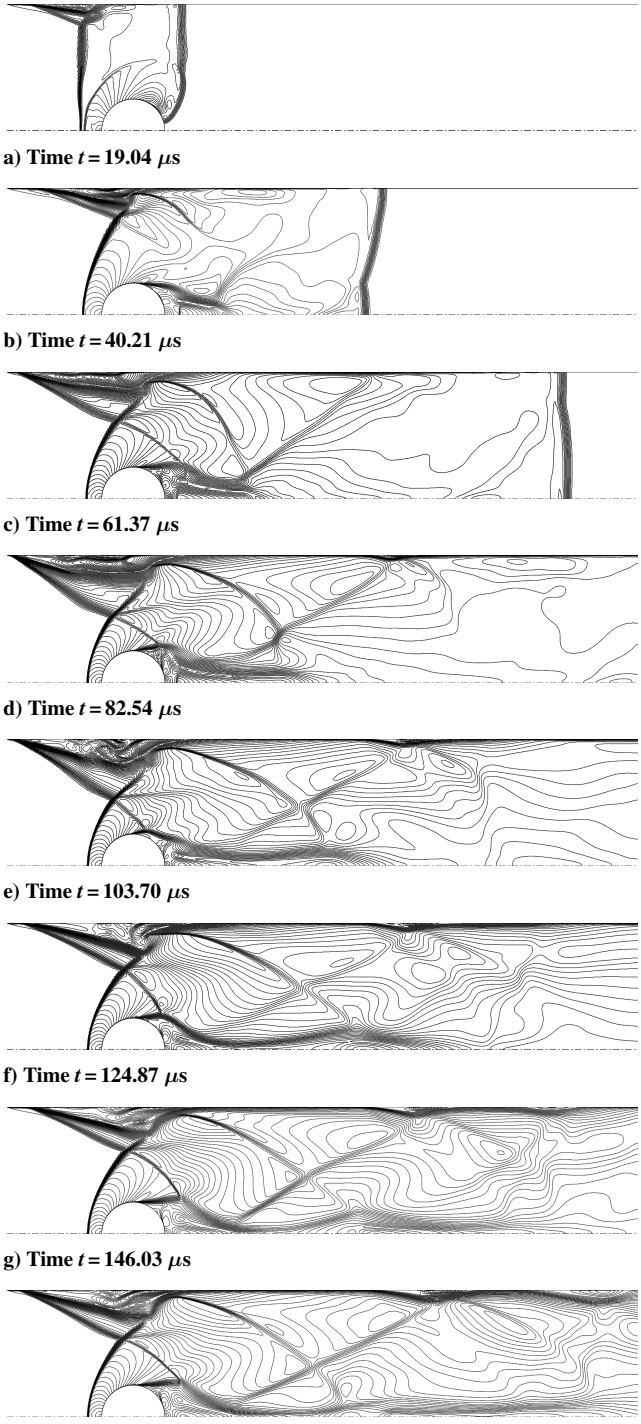

a) Time $t = 19.04$ μs

b) Time $t = 40.21$ μs

c) Time $t = 61.37$ μs

d) Time $t = 82.54$ μs

e) Time $t = 103.70$ μs

f) Time $t = 124.87$ μs

g) Time $t = 146.03$ μs

h) Time $t = 167.19$ μs

Fig. 14 Mach number contours for time-accurate calculation of case with CBR = 1/4 with solid wall as upper domain boundary; shown is the flowfield initialization by shock wave moving through the domain, Mach number contour level represents step of $\Delta M = 0.1$.

The overall thrust potential for all channel blockages, given in Fig. 18b, indicates that positive thrust potential at the end of the domain can only be achieved for CBRs in the range from 1/12 to 1/4, with the maximum of 140.3 sN/kg at the exit plane of the duct obtained for CBR = 1/9. The maximum thrust potential of 150.5 sN/kg along the duct is at a streamwise position of $x = 0.0675$ m, or 3.25 reference diameters from the inflow plane of the duct. This is the position where the oblique shock wave, caused by the reflection of the bow shock originating in front ot the blunt body at the upper boundary of the domain, is reflected at the symmetry plane through the center of the blunt body (Fig. 9e) and causes a decrease

a) Time $t = 19.05$ μs

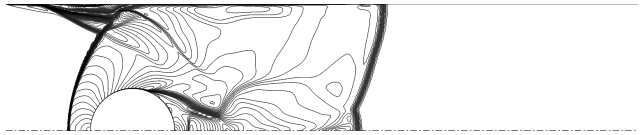

b) Time $t = 40.20$ μs

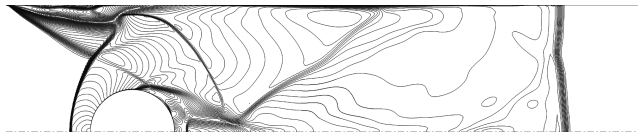

c) Time $t = 61.36$ μs

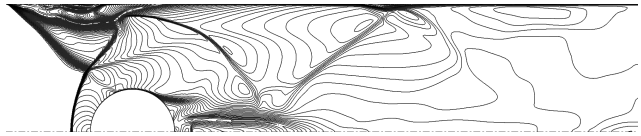

d) Time $t = 82.53$ μs

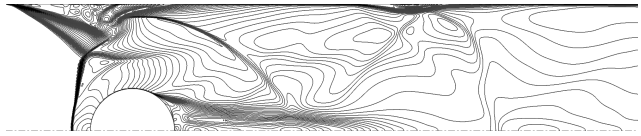

e) Time $t = 103.69$ μs

f) Time $t = 124.85$ μs

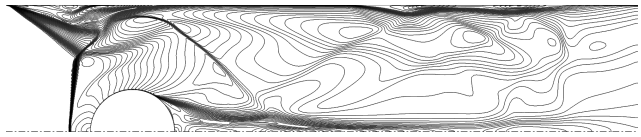

g) Time $t = 145.81$ μs

h) Time $t = 166.97$ μs

Fig. 15 Mach number contours for time-accurate calculation of case with CBR = 1/3 with solid wall as upper domain boundary; flowfield initialization by shock wave moving through the domain; Mach number contour level represents step of $\Delta M = 0.1$.

a) Time $t = 198.94$ μs

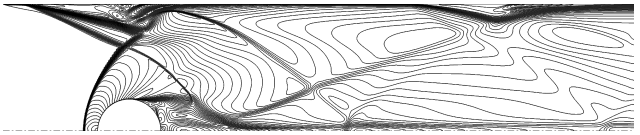

b) Time $t = 397.88$ μs

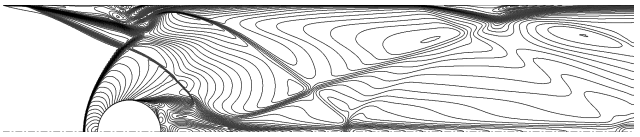

c) Time $t = 596.82$ μs

d) Time $t = 795.76$ μs

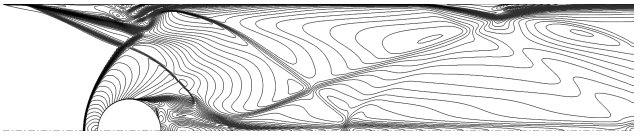

e) Time $t = 994.70$ μs

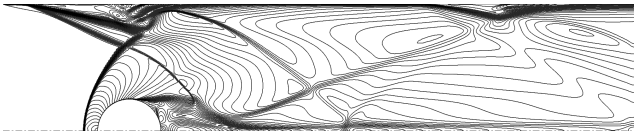

f) Steady-state result

Fig. 16 Mach number contours for time-accurate calculation of case with CBR = 1/4 with solid wall as upper domain boundary; Mach number contour level represents step of $\Delta M = 0.1$.

in thrust potential. In the design process of an entire scramjet engine, the inflow boundary of the nozzle would ideally be positioned upstream of this position to utilize the maximum thrust potential available.

The next parameter studied was the heat of reaction Δh_r released, which is defined as the amount of heat interaction required to bring the products back to the same temperature as the reactants. This is a theoretical process that occurs under constant pressure and with frozen chemistry, as outlined by Oates.[22] Therefore, the products will not change their chemical composition, which implies that the mass fractions will remain the same even when the temperature decreases. Hence,

$$\Delta h_r = \frac{1}{\dot{m}} \left\{ \iint_{\Gamma_{\text{outflow}}} \rho \boldsymbol{u} \cdot \boldsymbol{n} \sum_{i=1}^{N_s} Y_i h_i \Big|_{T_{\text{inflow}}} \mathrm{d}\Gamma - \iint_{\Gamma_{\text{inflow}}} \rho \boldsymbol{u} \cdot \boldsymbol{n} \sum_{i=1}^{N_s} Y_i h_i \Big|_{T_{\text{inflow}}} \mathrm{d}\Gamma \right\} \tag{26}$$

with the mass flux $\dot{m}$, the control volume surface Γ, and surface normal vector $\boldsymbol{n}$. This quantity is normalized by the product of specific heat at constant pressure and temperature of the combustor inflow $c_{p\infty} \cdot T_\infty$, using $c_{p\infty} = 1472.2$ J/(kg · K) and $T_\infty = 700$ K, corresponding to the second Damköhler number (see Ref. 23). According to Fig. 19, the maximum heat release and, therefore, optimum configurations, can be found around the CBR of 1/6 for both cases, with a symmetry plane and a solid wall at constant temperature as the upper domain boundary. The heat release for the case with a solid boundary is slightly larger than that with a symmetry plane as upper domain boundary and the optimum of the normalized heat release reaches a value of almost 1.6. Furthermore, the true optimum for both configurations can be expected somewhere between the CBRs of one-ninth and one-sixth. This assumption is valid especially for the case with a symmetry plane as an upper boundary because the heat release for the CBR of one-ninth and one-sixth are almost the

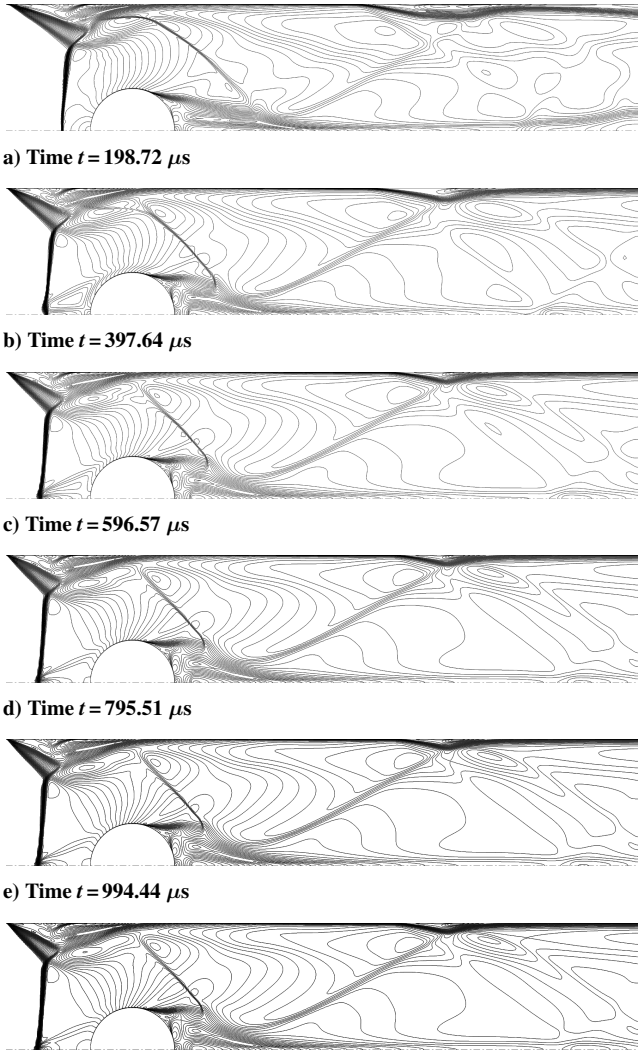

a) Time $t = 198.72\ \mu s$

b) Time $t = 397.64\ \mu s$

c) Time $t = 596.57\ \mu s$

d) Time $t = 795.51\ \mu s$

e) Time $t = 994.44\ \mu s$

f) Steady-state result

Fig. 17 Mach number contours for time-accurate calculation of case with CBR = 1/3 with solid wall as upper domain boundary; Mach number contour level represents step of $\Delta M = 0.1$.

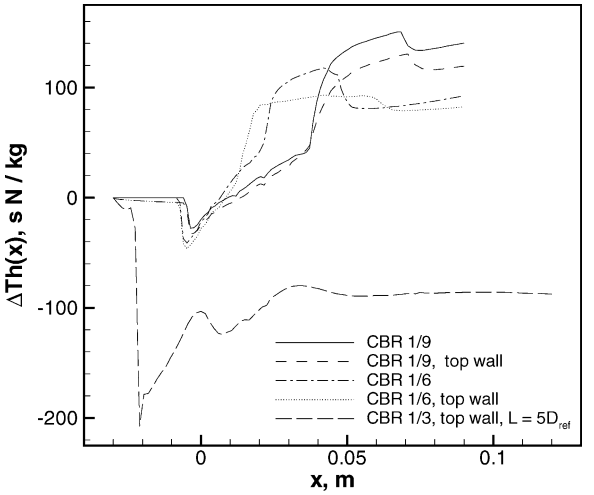

a) Along duct for selected cases

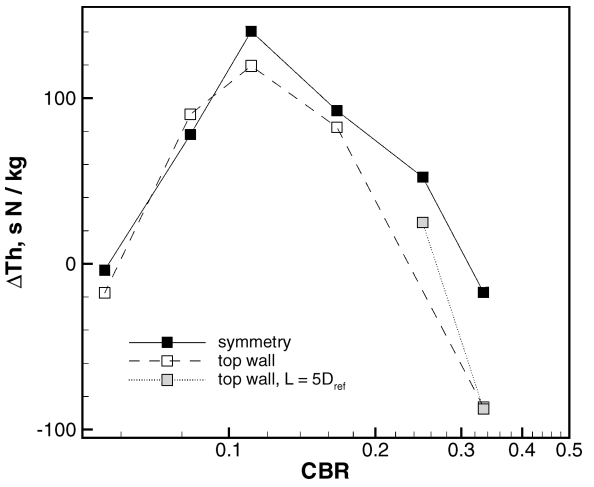

b) Different channel blockages

Fig. 18 Thrust potential for planes normal to the inflow direction a) along duct for selected CBRs and b) at exit plane for all CBRs; exit plane corresponding to the duct is taken to be eight times its height.

same. A comparison of the two setups, one with symmetry plane and one with a solid wall as an upper domain boundary, and their results for different CBRs are worth mentioning: For the smallest channel blockage of 1/18, and then again for 1/9, both setups produce nearly identical heat release. In the case of a channel blockage of 1/12, the case with a solid wall produces significantly higher heat release, and in the case of 1/6, slightly higher heat release. Flow with the extensive normal detonation wave for the configuration with the solid wall as the upper boundary then reduces the heat release for the largest CBR of 1/3, when compared to the configuration with symmetry plane. The longer residency time of the gas in the case of the domain with extended length $L = 5D_{\text{ref}}$, when compared with the domain with standard length $L = 4D_{\text{ref}}$, explains the slight increase in heat release for the case with channel blockage 1/3 and a solid upper wall. This allows the reaction to progress more toward the equilibrium state and increases the heat released.

In the ideal situation that all hydrogen and oxygen is converted into water, its mass fraction would be $Y_{\text{H}_2\text{O}} = 0.257$. Based on the heat of formation at standard conditions, this would yield a maximum heat release of 3.452 MJ/kg, or, normalized by $c_{p\infty} \cdot T_\infty$, a heat release of 3.35, more than double the heat release realized by the blunt-body generated combustion.

A complete analysis of the results also requires knowledge of the change of the water mass fraction, shown in Fig. 20. The water mass flux at the outflow boundary is integrated and divided by the overall mass flux to obtain the water mass fraction at the outflow. Because the increased channel blockage yields higher temperature levels, intermediate combustion products are favored over water, and, hence, the water mass fraction reduces again significantly for channel blockage ratios above 1/6.

The similarity of heat release for the smallest CBR of 1/18 for both configurations, with either a symmetry plane or a solid wall as an upper boundary, results because in both cases the combustion does not cover the entire channel height.

For the next higher CBR of 1/12, a clear difference between the two configurations can be observed. As shown in the preceding section, for this channel blockage, the solid upper wall causes an additional combustion zone that is not present in the case of a symmetry plane. This influences the water production in the same way as the heat release, as shown in Fig. 20.

Whereas for the CBR of 1/9 the resulting water mass fractions are nearly identical for both configurations, for the CBR of 1/6 it is slightly higher when a solid wall is present as an upper boundary.

In the case of the highest CBR of 1/3 the water production for the configuration with a solid wall as an upper domain boundary is lower than that with a symmetry plane because of the higher temperature levels due to the large normal shock wave standing in front of the blunt body, yielding high drag and low heat release.

Given the range of CBRs examined for the two configurations with a symmetry plane and a solid wall as upper domain boundaries, the results for the heat release and the water mass fraction correspond well with each other.

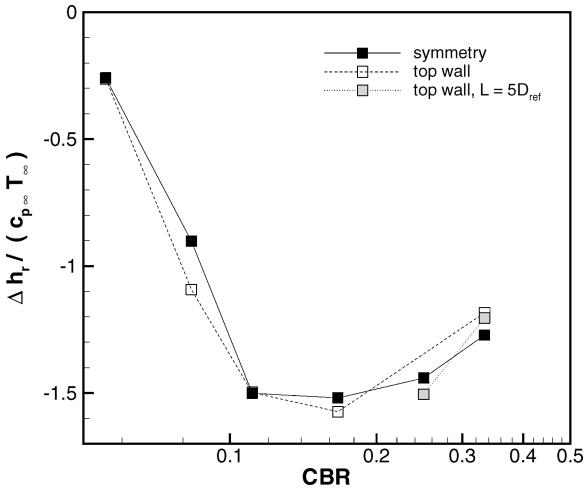

Fig. 19 Heat of reaction for different CBRs with symmetry plane and solid wall as upper domain boundaries, normalized by $c_{p\infty} \cdot T_\infty$ for inflow conditions.

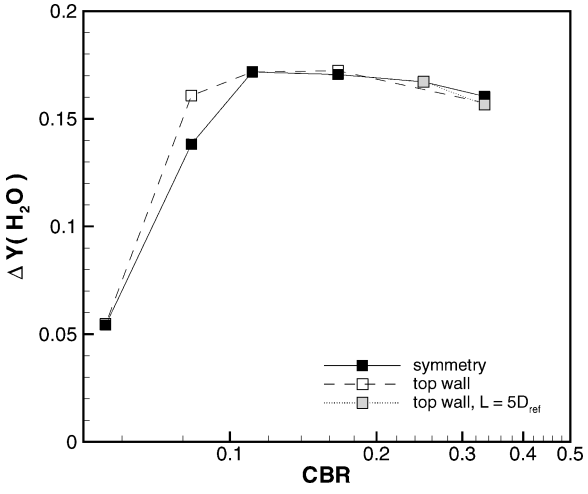

Fig. 20 Changes of water mass fractions for different CBRs with symmetry plane and solid wall as upper domain boundaries from inflow to outflow.

Conclusions

Blunt-body generated shock and detonation-induced combustion as applied to scramjet propulsion has been simulated with an unsteady implicit finite volume method, validated with experimental, numerical, and theoretical data, and is presented in this paper. A parameter study varying the CBR from 1/18 to 1/3 in a constant area channel flow with either a symmetry plane or a solid wall limiting the upper domain boundary has been performed.

All CBRs examined were found to be stable, and the optimum channel blockage with respect to heat released was found to be 1/6 in both cases. For small channel blockages, hydrogen remains unused, and for higher channel blockages strong shock systems and resulting high temperatures, decreasing water formation, degrade the heat release. The highest increase in thrust potential was observed for a CBR of 1/9, which is below that of the maximum heat release, because higher losses for the channel blockage with optimum heat release reduce the benefits of heat release more than in the case of the smaller channel blockage 1/9.

For the highest channel blockage studied, CBR = 1/3, a symmetry plane as an upper boundary of the domain resulted in a Mach stem reflection, whereas for lower channel blockages a regular reflection was obtained. When the symmetry plane at the upper boundary of the domain was replaced by a solid wall, a normal detonation wave formed in front of the blunt body, whereas for lower channel blockages a bow shock was observed.

The results presented here demonstrate the potential of blunt-body generated combustion for hypersonic propulsion, and future work will include an optimization of the shape of the blunt bodies, the consideration of turbulence, and the analysis of an entire scramjet engine based on this concept.

Acknowledgments

The Department of Aeronautics at Imperial College London and the Department of Mathematics at the University of Bristol are gratefully acknowledged for providing substantial computational time on their parallel computers. Various advice with respect to computing related issues, especially the implementation of efficient parallel code, by Ian Stewart is gratefully acknowledged.

References

[1]Dudebout, R., Sislian, J. P., and Oppitz, R., "Numerical Simulation of Hypersonic Shock-Induced Combustion Ramjets," *Journal of Propulsion and Power*, Vol. 16, No. 6, 1998, pp. 869–879.

[2]Clutter, J. K., "Computation of High-Speed Reacting Flows," Ph.D. Dissertation, Dept. of Mechanical and Aerospace Engineering, Univ. of Florida, Crainesville, FL, May 1997.

[3]Lehr, H. F., "Experiments on Shock-Induced Combustion," *Astronautica Acta*, Vol. 17, Nos. 4–5, Sept. 1972, pp. 589–597.

[4]Kasahara, J., Fujiwara, T., Endo, T., and Arai, T., "Chapman–Jouguet Oblique Detonation Structure Around Hypersonic Projectiles," *AIAA Journal*, Vol. 39, No. 8, 2001, pp. 1553–1561.

[5]Warnatz, J., and Maas, U., *Technische Verbrennung*, Springer, Barlin/Heidelberg, 1993, Chap. 5.

[6]Williams, F. A., *Combustion Theory*, 2nd ed., Benjamin/Cummings, Menlo Park, CA, 1985, Appendix E.

[7]McBride, B. J., Gordon, S., and Reno, M. A., "Coefficients for Calculating Thermodynamic and Transport Properties of Individual Species," NASA TM 4513, Oct. 1993.

[8]Hirschfelder, J. O., Curtiss, C. F., and Bird, R. B., Transport Phenomena of Dilute Gases, Wiley, New York, 1954, Chap. 8.

[9]Yee, H. C., Klopfer, G. H., and Montagné, J.-L., "High-Resolution Shock-Capturing Schemes for Inviscid and Viscous Hypersonic Flows," *Journal of Computational Physics*, Vol. 88, No. 1, May 1990, pp. 31–61.

[10]Shuen, J.-S., Liou, M.-S., and van Leer, B., "Inviscid Flux-Splitting Algorithms for Real Gases with Non-Equilibrium Chemistry," *Journal of Computational Physics*, Vol. 90, No. 2, Oct. 1990, pp. 371–395.

[11]Choi, J.-Y., Jeung, I.-S., and Yoon, Y., "Computational Fluid Dynamics Algorithms for Unsteady Shock-Induced Combustion, Part 1: Validation," *AIAA Journal*, Vol. 38, No. 7, 2000, pp. 1179–1195.

[12]Shuen, J.-S., "Upwind Differencing and LU Factorization for Chemical Non-Equilibrium Navier–Stokes Equations," *Journal of Computational Physics*, Vol. 99, No. 2, April 1992, pp. 233–250.

[13]Jameson, A., and Turkel, E., "Implicit Schemes and LU Decompositions," *Mathematics of Computation*, Vol. 37, No. 156, 1981, pp. 385–397.

[14]Ess, P. R., "Numerical Simulation of Blunt-Body Generated Detonation Waves in Viscous Hypersonic Ducted Flows," Ph.D. Dissertation, Dept. of Aerospace Engineering, Univ. of Bristol, Bristol, England, U.K., May 2003.

[15]Kunz, R. F., and Lakshminarayana, B., "Stability of Explicit Navier–Stokes Procedures Using k–ϵ and k–ϵ/Algebraic Reynolds Stress Turbulence Models," *Journal of Computational Physics*, Vol. 103, No. 1, Nov. 1992, pp. 141–159.

[16]Lawrence, S. L., Tannehill, J. C., and Chaussee, D. S., "An Upwind Algorithm for the Parabolized Navier–Stokes Equations," AIAA Paper 86-1117, May 1986.

[17]Sislian, J. P., Dudebout, R., and Oppitz, R., "Inviscid On-Design Propulsive Characteristics of Hypersonic Shock-Induced Combustion Ramjets," UTIAS TR 352, Inst. for Aerospace Studies, Univ. of Toronto, Toronto, Feb. 1997.

[18]Jachimowski, C. J., "An Analytical Study of the Hydrogen–Air Reaction Mechanism with Application to Scramjet Combustion," NASA TP 2791, Feb. 1988.

[19]Anderson, J. D., Jr., *Hypersonic and High Temperature Gas Dynamics*, McGraw–Hill, New York, 1989, Chaps. 6–8.

[20]Choi, J.-Y., Jeung, I.-S., and Yoon, Y., "Unsteady-State Simulation of Model Ram Accelerator in Expansion Tube," *AIAA Journal*, Vol. 37, No. 5, 1999, pp. 537–543.

[21]Riggins, D. W., McClinton, C. R., and Vitt, P. H., "Thrust Losses in Hypersonic Engines Part 1: Methodology," *Journal of Propulsion and Power*, Vol. 13, No. 2, 1997, pp. 281–287.

[22]Oates, G. C., *Aerothermodynamics of Gas Turbine and Rocket Propulsion*, AIAA Education Series, AIAA, Washington, DC, 1988, Chap. 3.5.

[23]Pratt, D. T., Humphrey, J. W., and Glenn, D. E., "Morphology of Standing Oblique Detonation Waves," *Journal of Propulsion and Power*, Vol. 7, No. 5, 1991, pp. 837–845.